RMetS

Royal Meteorological Society

Numerical discretization and subgrid-scale model effects on large-eddy simulations of a stable boundary layer

Georgios Matheou*

Jet Propulsion Laboratory, California Institute of Technology, Pasadena, CA, USA

*Correspondence to: G. Matheou, Jet Propulsion Laboratory, California Institute of Technology, 4800 Oak Grove Drive, Pasadena, CA 91109. E-mail: georgios.matheou@jpl.nasa.gov

Aspects of a large-eddy simulation (LES) model performance are investigated in simulations of a moderately stable boundary layer. The LES utilizes the constant-coefficient Smagorinsky–Lilly subgrid-scale (SGS) closure. Three model parameters are considered: grid spacing, SGS model constant and order of accuracy (resolving power) of the advection discretization. Second-, fourth- and sixth-order fully conservative non-dissipative advection schemes are examined. All three model parameters considered significantly affect the LES results. Depending on the value of the model constant, two main error-producing mechanisms are identified. For high values of the model constant, spurious turbulence collapse, either during the short period of model spin-up, or for the entire simulation duration, is observed. Even though this spurious model characteristic was previously documented, and perhaps expected for low-resolution simulations, it depends on the order of the advection discretization, implying a significant discretization and SGS closure interaction. For low values of the model constant, numerical discretization errors dominate, leading to accumulation of energy at small scales and over-prediction of the magnitude of the surface heat flux. Differences in potential temperature profiles are well correlated with the surface heat flux. Overall, the fourth- and sixth-order schemes perform significantly better than the second-order scheme. The differences between the fourth- and sixth-order schemes are relatively small and the increased computational expense of the sixth-order scheme may not be effective in most applications, at least for the low-order statistics considered in this study. Even though the results of the Smagorinsky–Lilly closure show persistent dependence on all model parameters examined, for several parameter combinations the differences with respect to a reference simulation are small. Thus, in contrast to the conclusions of previous studies, the closure can accurately capture moderately stable flows.

Key Words: large-eddy simulation; numerical methods; stable boundary layer; Smagorinsky–Lilly SGS model; grid resolution

Received 28 September 2015; Revised 18 July 2016; Accepted 25 July 2016; Published online in Wiley Online Library

1. Introduction

In stably stratified flows, vertical motions are suppressed because vertical displacements require the expenditure of potential energy. In a turbulent flow, this interplay between kinetic and potential energy results in confinement and reduction of the vertical energetic scale, reduced mixing, and increased anisotropy (e.g. Fernando, 1991; Riley and Lelong, 2000; Ivey *et al.*, 2008). Stable stratification generates internal flow scales, e.g. the Ozmidov or buoyancy scales, which significantly affect the turbulent dynamics (e.g. Zilitinkevich *et al.*, 2008; Chung and Matheou, 2012).

The presence of these internal flow scales can reduce the effectiveness of modelling methods such as large-eddy simulation (LES), which rely on explicitly capturing a wide range of turbulent motions, because the ratio of the energetic flow scale to the grid size decreases. Although it is difficult to unequivocally establish

this statement, LES of neutral and convective flows has been widespread and fairly successful since the early LES attempts. Simple closures based on Smagorinsky (1963) and Lilly (1962)-type parametrizations captured essential flow characteristics, even in flows that include capping inversions (e.g. Deardorff, 1970; Sommeria, 1976; Sommeria and Deardorff, 1977; Schmidt and Schumann, 1989; Cuijpers and Duynkerke, 1993).

In contrast, the LES model intercomparison study of a stable boundary layer of Beare *et al.* (2006) shows a relatively large spread in model results, even for bulk quantities such as the boundary-layer height. In addition, most of the models in Beare *et al.* (2006) and in the survey of Beare and MacVean (2004) do not use the simple Smagorinsky–TKE (turbulent kinetic energy) closures, but have more sophisticated formulations. All studies that accurately captured weakly and moderately stable boundary layers, and in some instances demonstrated grid convergence,

used an advanced turbulence closure (e.g. Kosovic and Curry, 2000; Esau, 2004; Basu and Porté-Agel, 2006; Stoll and Porté-Agel, 2008; Zhou and Chow, 2011; Huang and Bou-Zeid, 2013; Matheou and Chung, 2014). It is unexpected that LESs using the simple Smagorinsky closure were not able to capture weakly and moderately stable boundary layers and achieve grid convergence. Exceptions are the runs with the Smagorinsky closure of Matheou and Chung (2014) which show good resolution independence for grid lengths less than 4 m.

The aforementioned observations have led to the current study, which aims to re-examine the performance of LES with the simple Smagorinsky–Lilly closure for a moderately stable boundary layer and resolve some of the seeming inconsistencies.

The underlying hypothesis of the present investigation is that numerical discretization and turbulence closure parameters contributed to the poor past Smagorinsky results. Accordingly, improved model results can be obtained with modern numerical methods and, if required, some model tuning. The improvement of results will be assessed by comparison to a reference model solution, which indirectly assesses grid convergence.

The current study aims to elucidate the impact of these fundamental model choices in LES and to provide guidance for model design and simulation of stably stratified flows in general. Presently, only one boundary-layer case is considered. However, the results should be applicable to weakly and moderately stable boundary layers, i.e. with heights greater than the Obukhov length. In this stability regime, continuous turbulence is sustained in the boundary layer. In contrast, in strongly stratified flows, turbulence collapse (e.g. Schubert, 1977; Poulos and Burns, 2003; Mahrt, 2011; Chung and Matheou, 2012; Ansorge and Mellado, 2014) and bursts (e.g. Ohya *et al.*, 2008; Liu *et al.*, 2012; Van de Wiel *et al.*, 2012a) are expected and observed. These dynamics are not expected in the present flow, but for some combinations of model parameters turbulence collapse and bursts are observed in the current LES runs. Such spurious turbulence collapse in the present simulations is entirely a model artifact and has been observed (or suspected) and discussed in previous studies (Jiménez and Cuxart, 2005; Zhou and Chow, 2011; Van de Wiel *et al.*, 2012b).

The present study extends earlier investigations that examined the performance of LES with Smagorinsky-type subgrid-scale (SGS) closures in 'dry' (without water condensate) boundary layers. For instance, Brown *et al.* (2000) investigated the effects of advection discretization with respect to numerical dissipation and model constant in neutral and convective flows. Beare and MacVean (2004) and Beare *et al.* (2006) discussed resolution and model-constant sensitivity in stable boundary layers. Brown *et al.* (1994) carried out simulations with a refinement of the SGS closure that incorporates backscatter (Mason and Thomson, 1992), and showed improvements with respect to the standard purely dissipative formulation. In this article, a family of fully conservative non-dissipative finite-difference advection schemes of various orders is examined in combination with model constant values and grid resolution. Overall, the differences between the outcomes of the various model configurations are small, thus the best metric to quantify the variations of model results is with respect to a reference model run. A high-resolution reference run with the buoyancy-adjusted stretched-vortex SGS model (Pullin, 2000; Voelkl *et al.*, 2000; Chung and Matheou, 2014) is used. As will be discussed in section 4, the conclusions are not sensitive to the reference model, which is only used to construct quantitative comparison metrics.

2. Large-eddy simulation

2.1. Governing equations

The formulation of the LES model is fairly standard. However, for completeness, the governing equations and SGS model are briefly described here.

The LES model of Matheou and Chung (2014) is used. In LES the range of explicitly computed spatial (and temporal) flow scales is limited by applying a spatial filter. The LES code numerically integrates the filtered (density-weighted), anelastic approximation of the Navier–Stokes equations (Batchelor, 1953; Ogura and Phillips, 1962). Favre-filtered variables are defined as $\widetilde{\phi} \equiv \overline{\rho\phi}/\bar{\rho}$, where ρ is the density and the overbar denotes a spatially filtered variable. The conservation equations for mass, momentum, and potential temperature written on the f-plane and neglecting resolved-scale viscous terms, are, respectively,

$$\frac{\partial \bar{\rho}_0 \widetilde{u}_i}{\partial x_i} = 0, \tag{1}$$

$$\frac{\partial \bar{\rho}_0 \widetilde{u}_i}{\partial t} + \frac{\partial (\bar{\rho}_0 \widetilde{u}_i \widetilde{u}_j)}{\partial x_j} = -\theta_0 \bar{\rho}_0 \frac{\partial \bar{\pi}_2}{\partial x_i} + \delta_{i3} g \frac{\bar{\rho}_0 (\widetilde{\theta} - \langle\widetilde{\theta}\rangle_x)}{\theta_0}$$
$$- \epsilon_{ijk} \bar{\rho}_0 f_j (\widetilde{u}_k - u_{g,k}) - \frac{\partial \tau_{ij}}{\partial x_j}, \tag{2}$$

$$\frac{\partial \bar{\rho}_0 \widetilde{\theta}}{\partial t} + \frac{\partial \bar{\rho}_0 \widetilde{\theta} \widetilde{u}_j}{\partial x_j} = -\frac{\partial \sigma_j}{\partial x_j}. \tag{3}$$

The thermodynamic variables are decomposed into a constant potential temperature basic state, denoted by subscript 0, and a dynamic component. Accordingly, θ_0 is the constant basic-state potential temperature and $\rho_0(z)$ is the density. The subgrid terms τ_{ij} and σ_j represent the subgrid stress tensor and subgrid θ flux, respectively. u_i and $u_{g,i}$ are the Cartesian components of the velocity vector and geostrophic wind, respectively, and $f = [0, 0, f_3]$ is the Coriolis parameter. Buoyancy is proportional to deviations of potential temperature from its instantaneous horizontal average, $\langle\theta\rangle_x$. In the momentum equation (2), π_2 denotes the dynamic part of the Exner function, π, i.e.

$$\frac{\pi_0 + \pi_1 + \pi_2}{c_p} = \pi = \frac{T}{\theta} = \left(\frac{p}{p_{\text{ref}}}\right)^{\frac{R_d}{c_p}}, \tag{4}$$

which is used to enforce the anelastic constraint (1). The thermodynamic pressure, p, in each grid cell is computed from (4), the sum of the basic state Exner, $\pi_0(z)$, plus a contribution due to the deviation of the horizontal mean from the basic state, $\pi_1(t, z)$, and the dynamic $\pi_2(t, x, y, z)$ (Clark, 1979). π_1 balances the mean vertical acceleration: $d\pi_1/dz = \langle dw/dt\rangle_x/\theta_0$.

2.2. Subgrid-scale model

The SGS stress tensor and scalar flux are modelled using an eddy-diffusivity assumption

$$\tau_{ij} = -2\bar{\rho}_0 \nu_t \widetilde{D}_{ij}, \tag{5}$$

and

$$\sigma_j = -\bar{\rho}_0 \frac{\nu_t}{Pr_t} \frac{\partial \widetilde{\theta}}{\partial x_j}, \tag{6}$$

where $\widetilde{D}_{ij}$ is the zero-trace resolved-scale rate of strain tensor,

$$\widetilde{D}_{ij} = \frac{1}{2} \left(\frac{\partial \widetilde{u}_i}{\partial x_j} + \frac{\partial \widetilde{u}_j}{\partial x_i}\right) - \frac{1}{3} \delta_{ij} \frac{\partial \widetilde{u}_k}{\partial x_k}. \tag{7}$$

The eddy diffusivity for potential temperature is related to the SGS momentum diffusivity, ν_t, through the constant model turbulent Prandtl number, $Pr_t = 0.33$.

The closure originally introduced by Smagorinsky (1963) and Lilly (1966, 1967) is used to compute the turbulent diffusivity

$$\nu_t = \Delta^2 |\widetilde{D}| f_m(Ri), \tag{8}$$

where $\Delta = C_s \Delta x$ is the characteristic SGS length-scale, $|\widetilde{D}| = (2\widetilde{D}_{ij}\widetilde{D}_{ij})^{1/2}$ is the resolved-scale deformation, and f_m a stability correction function (Lilly, 1962),

$$
\begin{array}{ll}
f_m = (1 - Ri/Pr_t)^{1/2} & \text{for } Ri/Pr_t < 1 \\
f_m = 0 & \text{for } Ri/Pr_t \geq 1,
\end{array} \tag{9}
$$

where $Ri = N^2/|\widetilde{D}|^2$ is the gradient Richardson number and N is the buoyancy frequency.

Near the surface, the characteristic length-scale is modified to account for the confinement of the SGS eddies (Mason and Callen, 1986),

$$
\frac{1}{\Delta^2} = \frac{1}{(C_s \Delta x)^2} + \frac{1}{(\kappa_v z)^2}, \tag{10}
$$

where $\kappa_v = 0.4$ is the von Kármán constant and z the height from the surface.

The value of the model constant C_s has been the subject of many investigations since the first attempts to model three-dimensional turbulence (Lilly, 1966, 1967; Deardorff, 1971; Smagorinsky, 1993). Assuming homogeneous isotropic SGS turbulent flow and classical Kolmogorov (1941) scaling, Lilly (1966) showed that C_s can be theoretically determined.

A common assumption in LES is a balance between production and dissipation in a stationary SGS flow,

$$
\varepsilon = \frac{1}{2}\tau_{ij}\widetilde{D}_{ij}. \tag{11}
$$

Substituting the expression for the SGS stress tensor (5) for a neutrally stratified flow, the SGS dissipation is

$$
\varepsilon = \Delta^2 |\widetilde{D}/2|^{3/2}. \tag{12}
$$

The exact expression for the deformation $|\widetilde{D}|$ requires integration of the longitudinal and transverse velocity correlation functions (Lilly, 1966). Following the approximate derivation of Lilly (1967),

$$
\widetilde{D}_{ij}\widetilde{D}_{ij} = 3\left(\frac{\partial \widetilde{u}_1}{\partial x_1}\right)^2 + 6\left(\frac{\partial \widetilde{u}_2}{\partial x_1}\right)^2. \tag{13}
$$

Using the isotropic relation for the velocity derivatives and their relation to the so-called dissipation spectrum, the deformation can be written in terms of the turbulence spectrum, $E(k)$:

$$
\widetilde{D}_{ij}\widetilde{D}_{ij} = 15\left(\frac{\partial \widetilde{u}_1}{\partial x_1}\right)^2 = 2\int_0^{\pi/\Delta x} k^2 E(k)\,\mathrm{d}k. \tag{14}
$$

Assuming Kolmogorov scaling, $E(k) = C\varepsilon^{2/3}k^{-5/3}$,

$$
|\widetilde{D}|^2 \approx 3C\varepsilon^{2/3}\left(\frac{\pi}{\Delta x}\right)^{4/3}. \tag{15}
$$

Dissipation is eliminated using (12) and, after rearranging, the Smagorinsky constant depends only on the Kolmogorov constant:

$$
C_s = \frac{1}{\pi}\left(\frac{3}{2}C\right)^{-3/4}. \tag{16}
$$

For $C \approx 1.5$ (Saddoughi and Veeravalli, 1994) the model constant is $C_s \approx 0.173$.

The determination of C_s relies on two important elements. First, the existence of an inertial range near scale Δx. This implied grid resolution prerequisite in Smagorinsky–TKE type SGS models is discussed in Bryan et al. (2003) and Sullivan and Patton (2011). Second, Lilly (1967) interprets the wavenumber, $\pi/\Delta x$, in (14) as 'the largest wavenumber unambiguously representable on a finite difference mesh.' This is a rather stringent requirement,

because, as discussed in the next section, the resolving power of the different numerical schemes varies significantly with the largest well-resolved wavenumber differing by factors up to about four for the numerical schemes presently explored. For schemes with poor resolving efficiencies (see next section), the value of C_s should increase.

In the present simulations C_s is varied in the range 0.1–0.24. The C_s interval is centred at the theoretical value and encompasses most of the values used in the literature (e.g. Mason and Callen, 1986; Smagorinsky, 1993; Mason and Brown, 1999; Beare et al., 2006).

2.3. Numerical discretization

The LES implementation uses finite differences to discretize (1)–(3) on an Arakawa C (staggered) grid (Harlow and Welch, 1965; Arakawa and Lamb, 1977). An exact Poisson solver using discrete Fourier transforms is used to compute the modified pressure, π_2, in (2), and satisfy the anelastic constraint (Schumann, 1985). The same finite-difference scheme is used in all three spatial directions, i.e. the numerical discretization is isotropic.

Three approximations of the momentum and scalar advection terms, $\partial \rho_0 u_j u_i/\partial x_j$ and $\partial \rho_0 u_j \theta/\partial x_j$, respectively, are examined. The divergence form of the second-, fourth- and sixth-order accurate staggered-grid schemes of Morinishi et al. (1998) is used. All schemes are non-dissipative – all dissipation is supplied by the SGS closure – and are fully conservative. That is, discrete kinetic energy and scalar variance are conserved in a flow without any physical dissipation. The original formulation of Morinishi et al. (1998) is for a uniform density flow, and in the present LES the finite differences are modified to include the density. Accordingly, the conserved quantities are the mass-weighted variances, $\rho_0 u_i^2$ and $\rho_0 \theta^2$. The second-order scheme has identical properties to the second-order skew-symmetric form of Piacsek and Williams (1970) used in Brown et al. (1994).

Even though the advection schemes are identified by their formal order of accuracy, the order of accuracy is not a principal aspect of their performance in LES, because the numerical solution changes as the grid resolution is varied. In other words, $\widetilde{u}(t,x,y,z)$ is not converging towards a specific value as long as there are unresolved scales. Fourier error analysis is used to study the resolution characteristics of finite-difference schemes by considering a periodic function $f(x)$ and its corresponding Fourier coefficients $\widehat{f}(\kappa)$. The exact first derivative is $\mathrm{d}f/\mathrm{d}x = i\kappa\widehat{f}$, where $i = \sqrt{-1}$ is the imaginary unit and κ a scaled scalar wavenumber such that $\kappa\Delta x$ is $[0, \pi]$. A similar expression for the first derivative is obtained when it is approximated by a finite-difference scheme (e.g. Lomax et al., 2003, p 37),

$$
\frac{\delta f}{\delta x} = i\kappa^*\widehat{f}, \tag{17}
$$

where $\delta/\delta x$ denotes the approximation of the first derivative by the finite-difference scheme. For centred-difference schemes, κ^* is purely real and it approximates κ to the order of accuracy of the scheme. The functions $\kappa^*(\kappa)$ for the three schemes presently used are shown in Figure 1. The range of wavenumbers for which κ^* approximates the exact differentiation increases with the order of accuracy. This range of well-resolved Fourier modes is quantified by the resolving efficiency $r \equiv \kappa_r^*/\pi$, where κ_r^* is the largest well-resolved wavenumber for a given error tolerance $|\kappa^*(\kappa) - \kappa|/\kappa \leq \epsilon$ (Lele, 1992). For error tolerance $\epsilon = 0.01$, the resolving efficiencies of the three schemes are 0.05, 0.16, and 0.23. The resolving efficiency is independent of the grid resolution and only depends on the finite-difference scheme.

Another important property of the difference approximation is that differentiation acts as an implicit filter. The finite-difference approximation of the derivative of $f(x)$ can be expressed as the
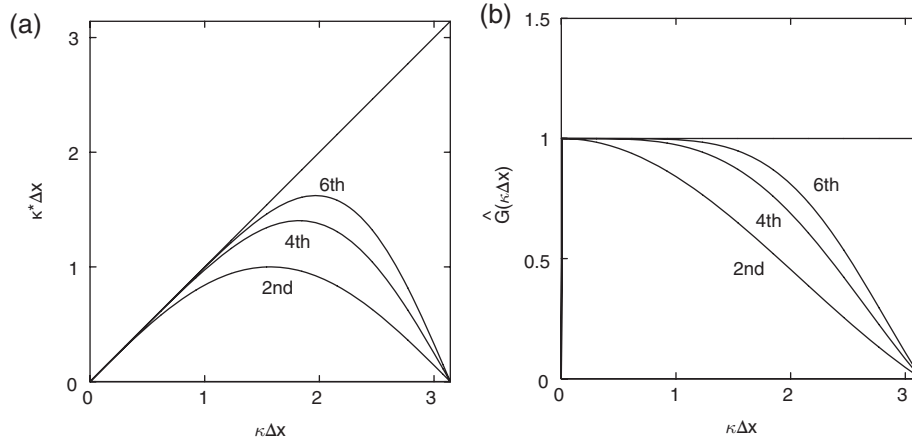
Figure 1. (a) Modified wavenumber and (b) implicit filter transfer function versus wavenumber for the three finite-differences schemes. The curves are labelled with the order of accuracy of each scheme.

exact derivative of a filtered variable with kernel G:

$$\frac{\delta f}{\delta x} = \frac{\mathrm{d}}{\mathrm{d}x}\int_{-\infty}^{\infty} G(x-x')f(x')\,\mathrm{d}x'. \quad (18)$$

The filter is determined by taking the Fourier transform,

$$i\kappa\widehat{f}\widehat{G}(\kappa) = i\kappa^{*}\widehat{f}. \quad (19)$$

The implicit filter corresponding to the differentiation scheme is

$$\widehat{G}(\kappa) = \frac{\kappa^{*}}{\kappa}. \quad (20)$$

Figure 1(b) shows the implicit filters, $\widehat{G}$, for the three schemes. As quantified by the resolving efficiencies, the band of well-resolved wavenumbers of the three schemes varies significantly. Most of the bandwidth improvement is between the second- and fourth-order schemes, with a relatively smaller gain attained by the sixth-order scheme.

An important limitation of Fourier analysis is that only linear periodic problems are considered, thus nonlinear errors, such as aliasing errors (e.g. Orszag, 1971), or the effects of boundary conditions, are not taken into account. As discussed in section 4, both these aspects are significant in the current simulations.

For all cases, regardless of the order of the advection scheme, second-order centred differences are used to approximate the spatial derivatives of the SGS model terms, including $|\widetilde{D}|$, using the discretization labeled 'SMV' in Matheou *et al.* (2011). Lilly (1966) suggests that the theoretical value of C_s must be somewhat adjusted when the continuous derivatives in the deformation, $|\widetilde{D}|$, are approximated by differences on the numerical grid. In the present study, because the discretization of the SGS terms remains the same regardless of the advection scheme order, any effects of the SGS-term derivative approximation should be inconsequential.

Periodic boundary conditions are used in the horizontal directions. The semi-discrete system of equations is advanced in time using the third-order Runge–Kutta of Spalart *et al.* (1991).

The LES code was successfully used in several previous studies (Matheou *et al.*, 2011; Inoue *et al.*, 2014; Matheou and Chung, 2014; Matheou and Bowman, 2016) and has been rigorously tested and validated.

2.4. Flow and simulation set-up

The simulations follow the set-up of the first Global Energy and Water Cycle Experiment (GEWEX) Atmospheric Boundary Layer Study (GABLS) model intercomparison study (Kosovic and Curry, 2000; Beare *et al.*, 2006). The initial potential temperature is constant $\theta(t=0) = 265\,\mathrm{K}$ up to $z=100\,\mathrm{m}$ and increases higher up with a lapse rate of $0.01\,\mathrm{K\,m^{-1}}$. The geostrophic wind is $u_g(z) = 8\,\mathrm{m\,s^{-1}}$ and the Coriolis parameter is $f = 1.39\times10^{-4}\,\mathrm{s^{-1}}$ (73°N latitude). The initial wind profile is identical to the geostrophic wind. The surface temperature is prescribed with $T(t=0) = 265\,\mathrm{K}$ and a surface cooling rate of $0.25\,\mathrm{K\,h^{-1}}$. The total water mixing ratio is assumed negligible with null surface latent heat flux. The reference potential temperature (2) is $\theta_0 = 263.5\,\mathrm{K}$.

The flow corresponds to a weakly stable arctic boundary layer, where the term weakly stable refers to conditions that can sustain turbulence without the creation of intermittent laminar–turbulent layers. The boundary layer becomes quasi-stationary after 8 h with a height which is about double the Obukhov length based on the surface fluxes.

A potential temperature perturbation is added to the initial condition to facilitate the transition of the horizontally uniform flow to turbulence (also discussed in section 4.4). Only the lowermost $z_r = 50\,\mathrm{m}$ levels are perturbed with fluctuations

$$\theta'(x,y,z) = \alpha\left(1 - z/z_r\right) r_\theta(x,y,z), \quad (21)$$

where r_θ are zero-horizontal-mean random numbers uniformly distributed in $[-0.5, 0.5]$; the amplitude is $\alpha = 0.2$. The turbulent flow is neutrally stratified at the beginning of the simulation with strong shear near the surface, thus the effects of stable stratification are not significant during the initial simulation spin-up and evolution of the boundary layer.

The domain height is 400 m, about double the boundary-layer height. A Rayleigh damping layer is applied above 300 m, to limit gravity wave reflection. The horizontal domain extent varies depending on the grid resolution (section 3.1). The smallest computational domain is 1 km long, about five times the boundary-layer height.

3. Methodology

3.1. Parametric study

The simulations span the three-dimensional parameter space of grid resolution $\Delta x = 4$–$8\,\mathrm{m}$, model constant $C_s = 0.1$–0.24, and advection order: second, fourth and sixth. The grid resolution increments are 1 m and C_s increments are 0.01 resulting in 120 runs for each advection order. For reference, the simulations in Beare *et al.* (2006) have grid resolutions in the range 1–12.5 m.

Three series of runs are carried out: a sweep of the parameter space using Monin–Obukhov similarity theory (MOST) for all surface fluxes (360 runs); a series using prescribed surface heat flux with fourth-order advection to investigate the effect of the lower boundary condition type (120 runs); and a series with a modified initial perturbation amplitude (2 runs). In addition,

three high-resolution runs with $\Delta x = 2$ m are performed, one with the reference stretched vortex model (SVM) closure and two with the Smagorinsky for $C_s = 0.18$ and 0.23. A total of 485 LES runs comprise the present study.

All simulations have a 400 m-high domain and 256×256 grid points in the horizontal directions (except the 2 m runs that have 512×512 grid points), which results in a variable horizontal domain extent. Fixing the domain size would restrict the number of grid points for the coarser runs. For the current investigation, it is important to allow a sufficient separation of flow scales for turbulence to evolve; thus it was deemed essential to have a minimum of 256 grid points or 1 km of domain length in each of the horizontal directions. A series of domain-size sensitivity simulations was carried out (not shown here) to verify the adequacy of the domain size. Wind and temperature profiles become domain-size independent for domains larger than 256 m and turbulent fluxes are identical in runs with domains larger than 512 m. All grids are isotropic, $\Delta x = \Delta y = \Delta z$.

In most simulations, MOST is applied locally, for each grid point separately, to estimate the surface fluxes of heat and momentum using Algorithm 2 of Basu *et al.* (2008). A series of runs is carried out using prescribed (time-dependent) heat fluxes obtained from the reference LES run, but with dynamically computed momentum fluxes using MOST.

A high-resolution run with the buoyancy-adjusted SVM (Pullin, 2000; Voelkl *et al.*, 2000; Chung and Matheou, 2014) is used for reference. LES results with SVM exhibit good agreement with theory and observations, and are resolution-independent for various boundary-layer flows, even for resolutions that are typically considered coarse (Matheou and Chung, 2014). Thus, the use of SVM as a reference model is justified.

The reference run uses the sixth-order advection scheme, SVM closure and 2 m resolution with $512 \times 512 \times 200$ grid points.

3.2. Flow statistics

Two types of flow statistics are considered: vertical profiles averaged in the horizontal directions and time in $t = 8-9$ h (when the boundary is in quasi-steady state), and time traces of the magnitude of the mean surface momentum flux, $(\langle uw \rangle_x^2 + \langle vw \rangle_x^2)^{1/2}$, surface sensible heat flux, $\langle w\theta \rangle_x$, and vertically integrated turbulent kinetic energy (TKE),

$$\frac{1}{2} \int_0^{L_z} \rho_0 (\langle u'^2 \rangle_x + \langle v'^2 \rangle_x + \langle w'^2 \rangle_x) \, dz,$$

where L_z is the LES domain height. The angle brackets with the subscript x, $\langle \cdot \rangle_x$, denote an instantaneous horizontal average whereas plain angle brackets, $\langle \cdot \rangle$, denote a horizontal–time average. Figures 2 and 3 show examples of profile and trace statistics, respectively.

3.3. Profile and surface flux error metrics

To understand the behaviour of the Smagorinsky runs as the LES model parameters vary, the reference run with the SVM, sixth-order advection and $\Delta x = 2$ m is used to form quantitative measures. The present comparison does not imply that the SVM run is identical to a fully resolved flow simulation (e.g. a direct numerical simulation) which is the absolute reference or 'truth'.

For the flow profiles, the 'error', or more appropriately the difference, between a Smagorinsky and the reference run is quantified by the l^2-norm,

$$l_\phi^2 = \left(\sum_k (\langle \phi(k) \rangle - \langle \phi(k)_{\text{ref}} \rangle)^2 \right)^{1/2}, \qquad (22)$$

for the discrete variable $\phi(k)$, $\phi = \{u, v, \theta\}$, where k is a $\Delta x = 2$ m run model-level index and the sum is over all model levels. All
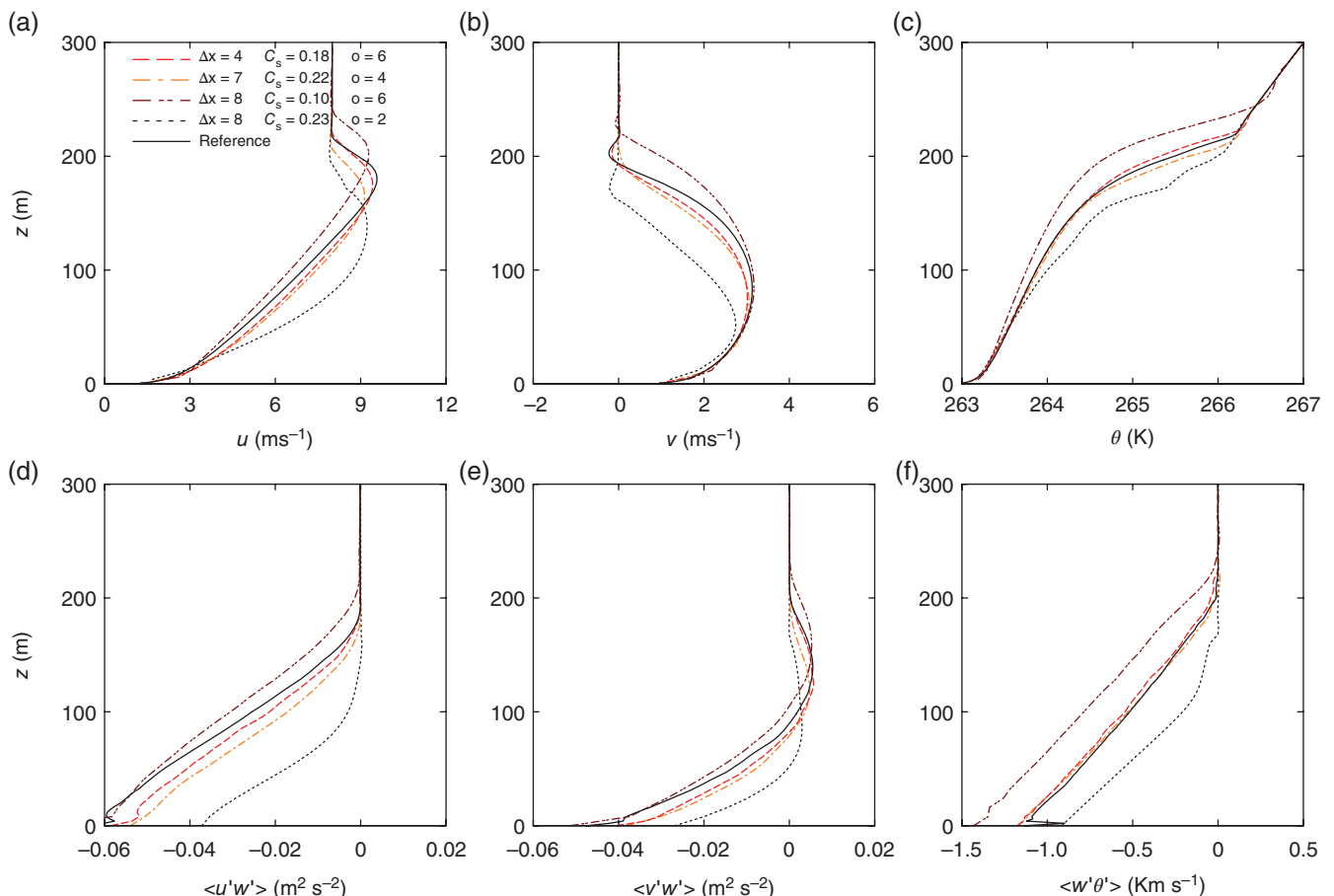
Figure 2. Profiles of (a) zonal and (b) meridional wind, and (c) potential temperature and their vertical turbulent fluxes (d)−(f) for four runs of the parametric study and the reference model. The legend symbols show the grid spacing (m), the value of the Smagorinsky constant C_s and the order of accuracy of the advection scheme.
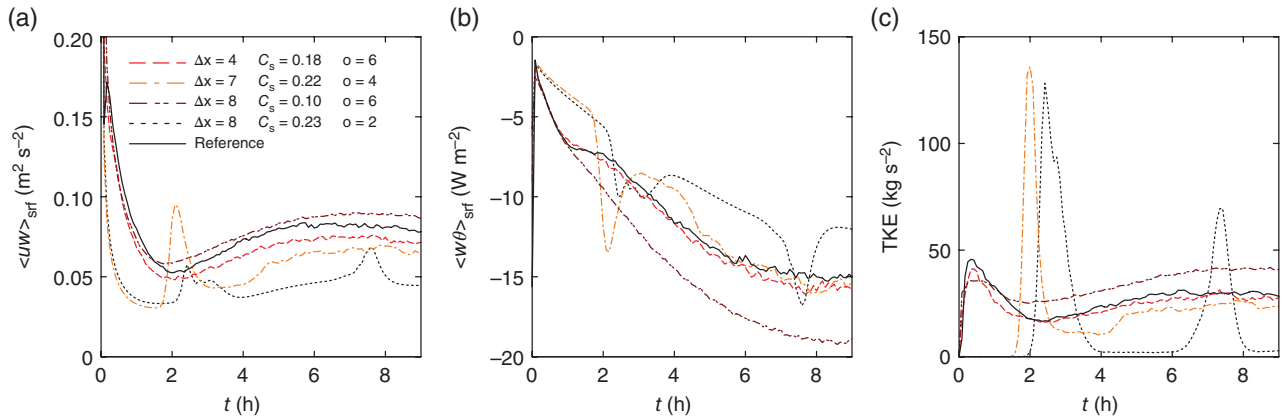
Figure 3. Time traces of (a) surface momentum flux, (b) surface heat flux and (c) vertically integrated turbulent kinetic energy (TKE) for the four runs shown in Figure 2 and the reference model. Momentum flux traces show the flux magnitude, $(\langle uw \rangle_x^2 + \langle vw \rangle_x^2)^{1/2}$. The spurious turbulence collapse is visible in the traces.

profiles are interpolated on the reference simulation grid such that all ϕ vectors have the same length. Polynomial interpolation corresponding to the order of the finite-difference approximation is used, i.e. different polynomial orders are used for each advection scheme order. Because the l^2-norm differences span a wide range of values, a logarithmic error scale is used for the wind components and potential temperature,

$$E_{\{u,v\}} = \log(l^2_{\{u,v\}}/U_g), \qquad (23)$$

$$E_\theta = \log(l^2_\theta/\theta_0), \qquad (24)$$

respectively, where $U_g = 8 \, \text{m s}^{-1}$ is the magnitude of the geostrophic wind and $\theta_0 = 263.5 \, \text{K}$ the reference potential temperature. The natural logarithm is used to form $E_{\{u,v,\theta\}}$, which depends on Δx, C_s, and the advection scheme. Even though the boundary-layer height is not directly considered, the normalized error E encapsulates boundary-layer height differences. As shown in Figure 2, most of the profile differences are because of different boundary-layer depths, particularly in the θ profiles. The direction of the difference in height, i.e. higher or lower with respect to the reference, can be inferred from the surface flux difference. The detailed dependence of the quasi-equilibrium boundary-layer height and profiles on the boundary conditions is discussed in several studies (e.g. Nieuwstadt, 1984; Derbyshire, 1990; Zilitinkevich and Mironov, 1996).

For the surface fluxes the difference,

$$d = \frac{1}{T} \int_0^T \langle w\phi \rangle_{x,\text{ref}} \, dt - \frac{1}{T} \int_0^T \langle w\phi \rangle_x \, dt, \qquad (25)$$

where $\langle w\phi \rangle_x$ is either the surface momentum $(\langle uw \rangle_x^2 + \langle vw \rangle_x^2)^{1/2}$ or heat flux $\langle w\theta \rangle_x$, is used to quantify the error. The flux differences are plotted based on (25) to preserve the sign and d has the units of the corresponding surface flux.

Using the l^2-norm and the mean surface flux difference has the advantage of reducing the difference between two runs to a single scalar value, which aids the comparison.

3.4. Spurious turbulence collapse flag

Figure 3 shows time traces of momentum and temperature surface fluxes, and vertically integrated TKE for a sample of four runs from the parametric study. The TKE traces of the run with $\Delta x = 8 \, \text{m}$, $C_s = 0.23$, and second-order advection show that turbulence cannot be continuously sustained in the boundary layer. The boundary layer exhibits a global turbulence collapse that is interjected by bursts of increased activity. Turbulence collapse and bursts alter the surface momentum and heat fluxes, which show similar spikes and smooth regions. Global turbulence collapse, i.e. entire boundary-layer laminarization, is clearly an invalid flow state and all such LES runs do not reproduce a realistic

flow. Global turbulence collapse is presently defined as periods after model spin-up ($t > 2 \, \text{h}$) when the vertically integrated TKE is nearly zero ($< 5 \, \text{kg s}^{-2}$), that is, the flow exhibits no fluctuations.

The TKE trace of the run with $\Delta x = 7 \, \text{m}$, $C_s = 0.22$, and fourth-order advection shows turbulence collapse during model spin-up with subsequent recovery for the remainder of the simulation. Similar features during the simulation spin-up can be observed in Figure 6 of Beare *et al.* (2006). The collapse during model spin-up, occurring in the first 2 h, does not invalidate the entire run, but may result in increased model errors. The error is mainly introduced through the modified surface fluxes of momentum and heat (Figure 3) since the initial collapse alters the time integral of drag and cooling of the boundary layer (when a temperature boundary condition is used). In other words, the comparison of two simulations at time t can be affected by this large deviation of surface fluxes, rather than the turbulent boundary-layer dynamics. The collapse during model spin-up can be affected by the initial perturbation and such effects are discussed in section 4.4. Also, effects of the type of boundary condition (prescribed surface temperature or its flux) are discussed in section 4.3. Turbulence collapse during model spin-up is defined as nearly zero ($< 5 \, \text{kg s}^{-2}$) vertically integrated TKE for $t < 0.5 \, \text{h}$.

A collapse flag or index is defined and each LES run is categorized as either exhibiting global turbulence collapse, turbulence collapse during model spin-up, or no collapse. Figure 4 shows the collapse flag for the three LES parameters: Δx, C_s, and advection order. Runs exhibiting collapse during model spin-up are a subset of the global collapse runs.

4. Results

4.1. Spurious turbulence collapse

Figure 4 shows the collapse flag for the three parameters Δx, C_s, and advection order. Each panel of Figure 4 corresponds to a different advection order, which is the only discrete variable of the parameter space. The flow statistics are expected to vary smoothly with respect to the continuous Δx and C_s variables, because of their role in the turbulent diffusivity. To aid the comparison of results, many of the figures show discrete values for each Δx–C_s pair, rather than contour plots that are expected for a continuously varying parameter space. In Figure 4, runs with global collapse are denoted by black fill colours, collapse during model spin-up by grey fill colours and white by always-turbulent simulations. Contours of $\Delta = C_s \Delta x$ are superimposed on the plots of Figure 4. Only a subset of runs, those with $C_s \geq 0.18$, are shown in Figure 4 because no collapse is observed for smaller C_s.

Perhaps as expected, Δx and C_s affect spurious turbulence collapse, with coarse simulations and higher C_s values, i.e. higher Δ, being more prone to collapse. However, the collapse flag does not follow the Δ contours and spurious turbulence collapse is confined to high C_s. The turbulence closure depends on Δ
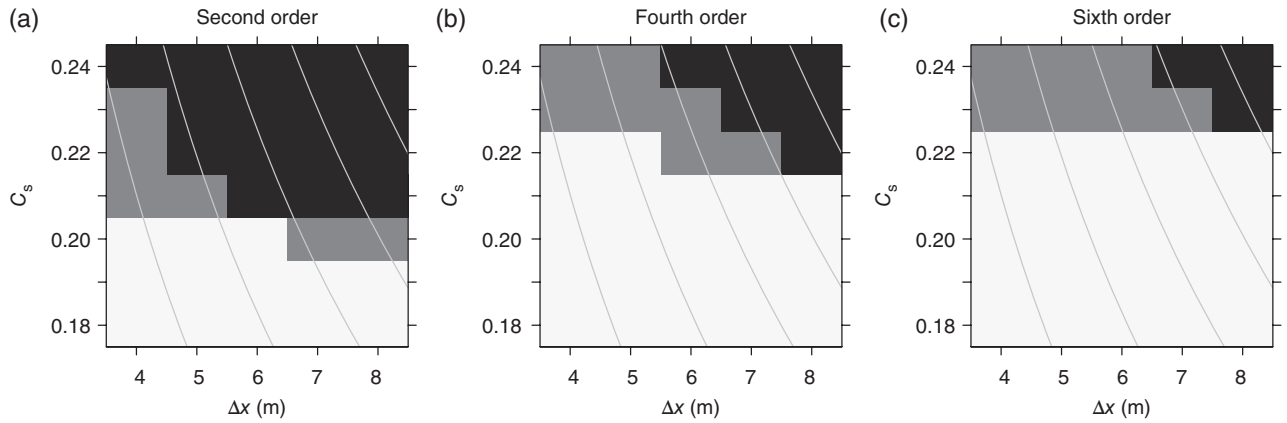
Figure 4. Turbulence collapse flag for (a) second-, (b) fourth- and (c) sixth-order advection. Black regions indicate global turbulence collapse, grey regions collapse during model spin-up, and white fully turbulent boundary layers. Grey curves denote constant $\Delta = C_s \Delta x$ contours.

whereas advection discretization errors only depend on Δx. In addition, the significant differences with respect to the advection scheme imply that the order of accuracy, i.e. the resolving efficiency, of the advection discretization has a significant impact. There is a direct effect of advection discretization on turbulence closure performance. Spurious turbulence collapse is confined to higher Δ for higher-order schemes. This interaction between numerics and turbulence closure has been observed and studied in neutrally stratified flows (Ghosal, 1996; Chow and Moin, 2003). The present results show that numerics–closure interactions in stably stratified flows are also significant with spurious turbulence collapse being an additional mechanism of model error.

4.2. Differences with respect to the reference model

The spurious turbulence collapse flag shown in Figure 4 is only one metric of model error. To quantify the quality of the simulations that sustain turbulence and explore the lower range of C_s, the error metrics with respect to the reference model (23–25) are used. Figures 5–7 show the differences of zonal and meridional wind, and potential temperature with respect to the reference

run. Figures 5–7 include runs that exhibit turbulence collapse to provide a comparison of the different error type magnitude.

The distribution of error is similar between the u and v wind components and, for most C_s values, does not monotonically decrease with grid resolution. The non-monotonic variation of flow statistics with respect to resolution in LES, although not well understood, is commonly observed, e.g. Figure 3 of Beare and MacVean (2004) and Figures 5 and 12 of Matheou and Chung (2014). In contrast, the potential temperature error decreases with resolution in the parameter range explored. Overall, the largest errors are observed when the second-order scheme is used. The fourth- and sixth-order schemes show similar values and distributions of the difference with respect to the reference run.

Figures 8 and 9 show surface flux differences, d, for momentum and temperature. The temperature error in Figure 7 is well-correlated to the surface heat flux difference shown in Figure 9. Because the surface fluxes are dynamically computed, this relation cannot result in a causal relationship, i.e. if θ errors are caused by the surface flux errors or the reverse. Similar to the wind errors, the momentum surface flux difference (Figure 8) increases with decreasing resolution for $C_s < 0.18$. This trend is reversed for
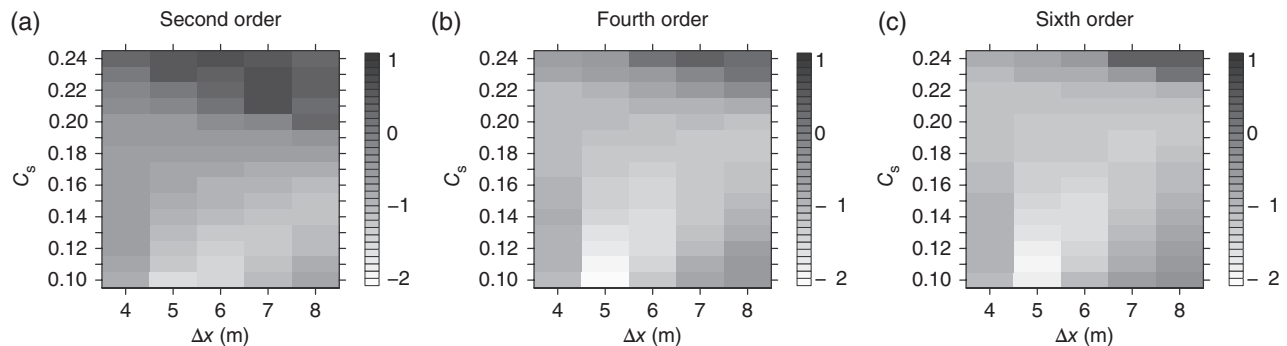
Figure 5. Logarithm of l^2-norm normalized difference of zonal wind with respect to the reference run for (a) second-order, (b) fourth-order and (c) sixth-order schemes.
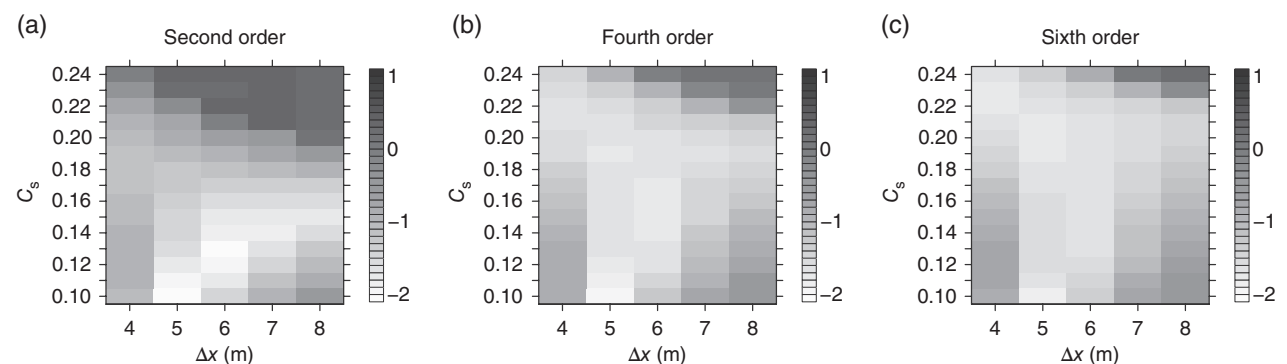
Figure 6. As Figure 5, but for meridional wind with respect to the reference run.
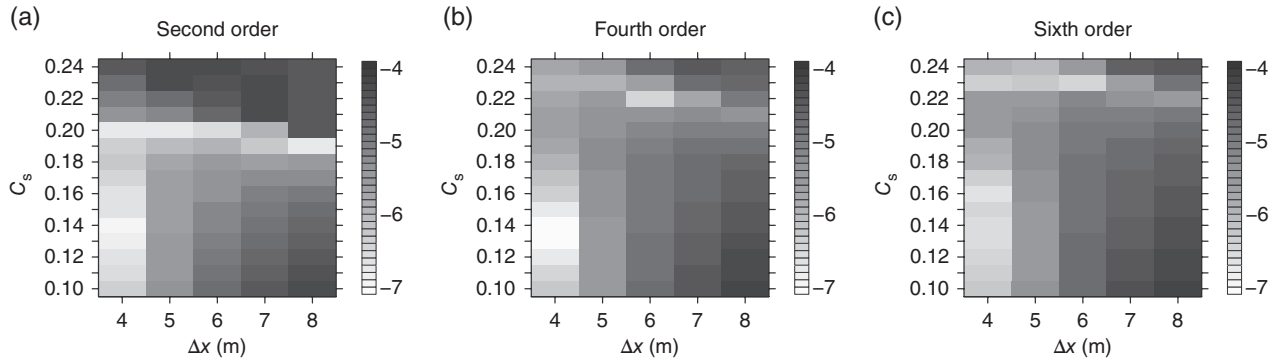
Figure 7. As Figure 5, but for potential temperature with respect to the reference run.
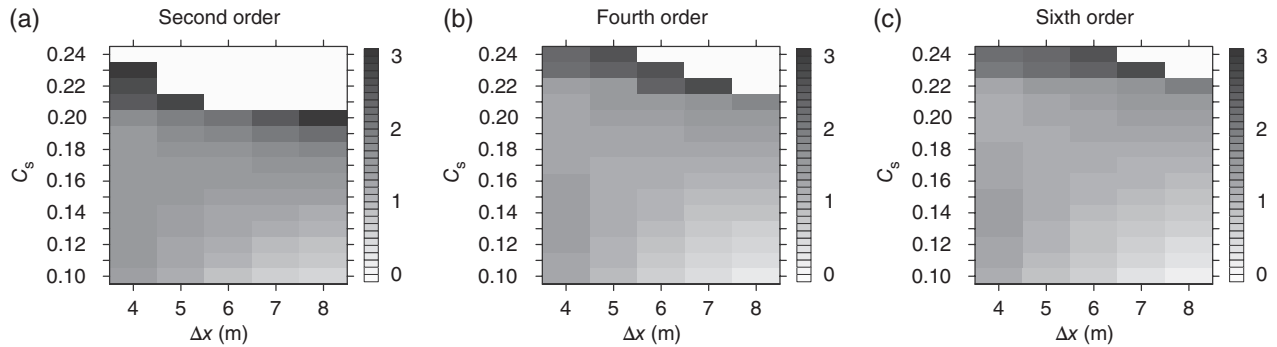
Figure 8. Difference (reference minus Smagorinsky run) of time-averaged momentum flux ($\times 10^{-2}\,\mathrm{m^2 s^{-2}}$). White areas correspond to regions of global spurious turbulence collapse.

$C_s > 0.18$: the momentum flux converges to the reference run with decreasing Δx. The heat flux errors also drift with respect to Δx, but always decrease in absolute value irrespective of C_s. The spectral analysis in section 4.5 provides further insight into the surface fluxes behaviour.

4.3. Prescribed sensible heat flux

To eliminate the feedback between boundary-layer turbulence and surface heat flux, an additional set of runs was carried out by prescribing the surface heat flux. The time-dependent sensible heat flux from the reference run (black continuous line in Figure 3(b)) is used uniformly in all surface grid cells of the Smagorinsky runs. The momentum flux is computed dynamically using MOST as before. Only runs with the fourth-order advection are performed with prescribed heat fluxes.

Even though the prescribed heat flux is largely consistent with the boundary-layer dynamics in the mean, it cannot adjust to the local spatial and temporal temperature fluctuations. This changes the overall behaviour of the flow. As shown in Figure 10, most of the runs show spurious turbulence collapse during model spin-up and the region of global collapse is expanded. The regime of collapse during model spin-up is expanded from $C_s > 0.22$ to $C_s > 0.14$. The profile difference plots of Figure 11 show altered distributions compared to (b) of Figures 5–7. The difference with respect to the reference runs is larger at finer resolutions and the difference distribution appears more random compared to the runs with temperature boundary condition. Basu *et al.* (2008) show that prescribing the surface heat flux should be avoided in very stable conditions. Although the present conditions are not part of the expected pathological regime for strongly stable boundary layers, significant model sensitivity is observed with respect to the type of surface boundary condition used.

4.4. Initial perturbation

The observed spurious global turbulence collapse is attributed to limitations of the turbulence closure and it is expected to be independent of the initial condition. In contrast, the turbulence collapse during model spin-up is directly affected by the initial condition. Because of the relatively high value of the geostrophic wind and the initially neutral lapse rate near the surface, the flow should develop shear instabilities and quickly transition to turbulence. The purpose of initial perturbation (21) is to introduce randomness, such that the flow quickly de-correlates from the initial condition, and not to induce the transition to turbulence. Accordingly, initial perturbations have very small amplitudes.

Deviating from initial perturbations aimed at only introducing randomness, three cases are carried out with double and four times the base perturbation amplitude $\alpha = 0.2$ of (21). The cases correspond to fourth-order advection, $C_s = 0.22$, and $\Delta x = 6$, 7 and 8 m. The base $\Delta x = 6$ and 7 m runs exhibit turbulence collapse during model spin-up and $\Delta x = 8$ m global collapse (Figure 4). Figure 12 shows the vertically integrated TKE traces for all runs. Doubling the perturbation amplitude results in essentially no change in the TKE traces. Runs with 4α do not exhibit collapse during model spin-up, but for $\Delta x = 8$ m, large TKE variations are observed.

Even though the increase of the initial perturbation amplitude appears to address the spurious turbulence collapse, it does not amount to a solution of the problem because it is an artificial introduction of potential energy which gets converted to kinetic energy after initialization. In other words, it alters the character of the initial-boundary value problem.

4.5. Spectral analysis and surface fluxes

The average flow statistics that form the error metrics and turbulence collapse flag do not take into account the multi-scale character of the turbulent flow. To gain insight into the energy distribution across scales, the spectra of zonal wind and potential temperature are considered. Of primary interest is the effects of C_s on the turbulence energy (and variance) cascade and the representation of small scales near the surface and aloft.

The one-dimensional energy spectra are computed by taking the two-dimensional Fourier transform of $u(x, y, z)$ at constant z, $\widehat{u}(k_x, k_y, z)$, and then averaging across k_y to form $E_{uu}(k_x, z)$, or similarly, $E_{\theta\theta}$ for the potential temperature spectrum. This
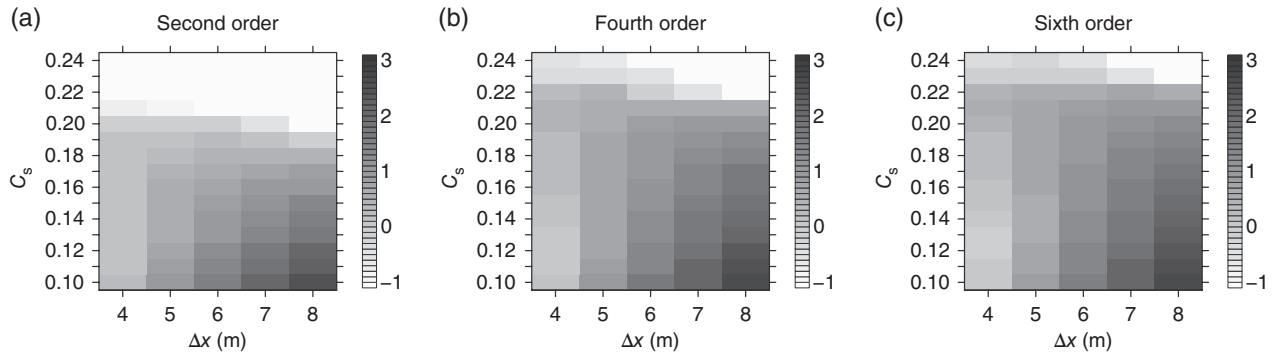
Figure 9. As Figure 8, but for time-averaged sensible heat flux (W m^{-2}).
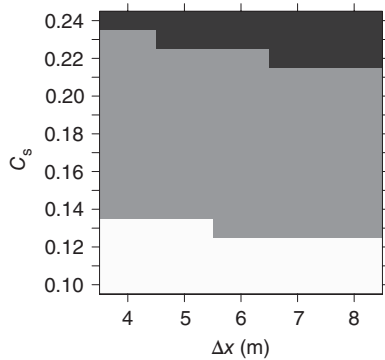
Figure 10. Turbulence collapse flag for runs with prescribed surface heat flux and fourth-order advection. Black regions indicate global turbulence collapse and grey regions collapse during model spin-up.

procedure reduces some of the aliasing of the y modes onto the low wavenumbers of the x direction, which is present when spectra are computed using one-dimensional transforms. All spectra are computed at the end of the run, $t = 9$ h, and no time averaging is performed, to avoid any masking of numerical errors. This results in somewhat noisy spectra, but their overall shape is readily discernible.

Figures 13 and 14 show the compensated spectra of u and θ for runs with $\Delta x = 4$ m and sixth-order advection at three heights: the first model half-level $z = \Delta z/2 = 2$ m, at $z = 30$ m, and $z = 100$ m at boundary-layer half-height. The compensated spectra show nearly inertial scaling, i.e. 'flat' regions, for $k_x z > 1$ and peak at about $k_x z = 1$ near the surface. As expected, C_s affects the high wavenumber range of both u and θ spectra, with higher C_s resulting in more damping of the fine-scale fluctuations (the eddy diffusivity depends on C_s^2). The effect of C_s appears to extend to the highest decade of wavenumbers, with energy accumulation before the final roll-off for the lowest C_s values. This is most evident at $z = 30$ m at about $k_x z \approx 10$ (Figures 13 and 14).

The roll-off of the spectra at the highest wavenumbers is due to the implicit filter of the finite differencing (18). Figure 15 shows this effect for runs with $\Delta x = 8$ m and $C_s = 0.18$. Because the domain is larger than the $\Delta x = 4$ m runs of Figure 14, leading to a broader scale separation, the spectra at $z = 100$ m of Figure 15 exhibit good inertial scaling.

The potential temperature spectra, particularly near the surface, show indications (the small 'hook' at the high-wavenumber end) of aliasing (Orszag, 1971). Aliasing is a form of numerical error caused by the nonlinear interactions of the quadratic term of the equations of motion and it is common in simulations of fluid flows (e.g. Donzis *et al.*, 2010; Chung and Matheou, 2012, 2014). Typically, in LES, the strong dissipation action of the SGS model at the smallest scales prevents the growth of aliasing errors. This grid-scale accumulation of energy is not discernible in the velocity spectra. Even though the magnitude of the grid-scale fluctuations is relatively small because of the SGS model dissipation and the finite-difference filter, the presence of increased numerical error at the lowermost grid level can affect the calculation of the surface

fluxes. The spectra in Figures 13 and 14 correspond to the finest resolution which exhibits the least amount of aliasing errors.

To assess the impact of grid-scale potential temperature numerical errors at the first model half-level, the probability density functions (pdfs) of the temperature difference between the first model half-level and surface, $\Delta\theta(t, x, y) = \theta(t, x, y, \Delta z/2) - \theta_{\text{srf}}(t)$, are shown in Figure 16 for runs with $\Delta x = 8$ m, $C_s = 0.1$–0.18 and sixth-order advection. The pdfs are computed at times $t = 1$, 2, and 3 h in order to explore the observed drift of the heat flux with respect to the reference run (run $\Delta x = 8$ m, $C_s = 0.1$, sixth-order in Figure 3; and Figure 9). The pdfs of $\Delta\theta$ become broader, particularly for larger $\Delta\theta$, as C_s decreases, which leads to more negative (larger in absolute value) heat fluxes. The surface heat flux, unlike the momentum flux, depends nonlinearly (cubic) with respect to $\Delta\theta$, e.g. Figure 2 of Basu *et al.* (2008) and related discussion therein. Presently, the boundary-layer height increases significantly when the surface flux magnitude is over-predicted, for instance, run $\Delta x = 8$ m, $C_s = 0.1$, and sixth-order advection in Figures 2 and 3. As shown in Figure 9, the drift of the surface heat flux is reduced as resolution increases and in cases with $C_s > 0.18$. Increased numerical errors result in broader steady-state $\Delta\theta$ distributions leading to different mean surfaces fluxes, even though the cooling rate, bulk boundary-layer temperature difference and surface flux computation method are identical. This is likely the reason for the variation of the surface flux in Figure 4 of Beare *et al.* (2006).

Overall, for the present parametric study, the spectral analysis suggests that $C_s < 0.18$ leads to increased numerical errors that manifest as accumulated energy (spectral 'bumps') at small scales in u and θ and aliasing for θ near the surface. Figures 5–7 show that, for some combinations of Δx and C_s, when $C_s < 0.18$ the differences with respect to the reference model can be small. However, the wind-field error does not monotonically decrease as Δx is reduced and it is likely that this behaviour is problem-dependent, e.g. depends on the atmospheric stability. In summary, C_s values near or somewhat larger than the theoretical, $C > 0.17$, yield the expected model behaviour: monotonic convergence with respect to Δx and inertial range scaling for $k_x z > 1$. Larger values of C_s can be used to control numerical errors, such as aliasing. However, high C_s in combination with coarse grid resolutions and low advection scheme resolving efficiencies can lead to spurious turbulence collapse.

4.6. Fine-scale simulations

Based on the conclusions of the parametric study, two additional runs with the Smagorinsky closure are carried out with an otherwise identical setup as the reference run, i.e. with the sixth-order advection and $\Delta x = 2$ m. $C_s = 0.18$ and 0.23 are used. The two Smagorinsky fine-scale simulations are a type of 'consistency check' to confirm that, for sufficiently high resolution and judicious model-parameter choices, the two SGS closures can yield similar results. Figures 17 and 18 compare the profiles and time traces with the SVM (reference) run. Overall, the agreement is good, but some differences and sensitivity to C_s remain,
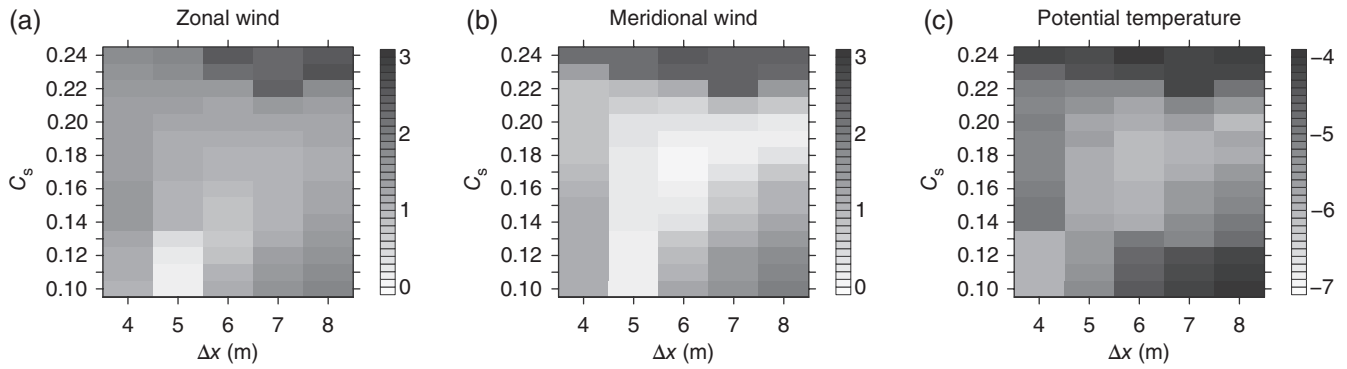
Figure 11. Logarithm of l^2-norm normalized difference of (a) zonal wind, (b) meridional wind and (c) potential temperature, for fourth-order advection and prescribed surface heat flux.
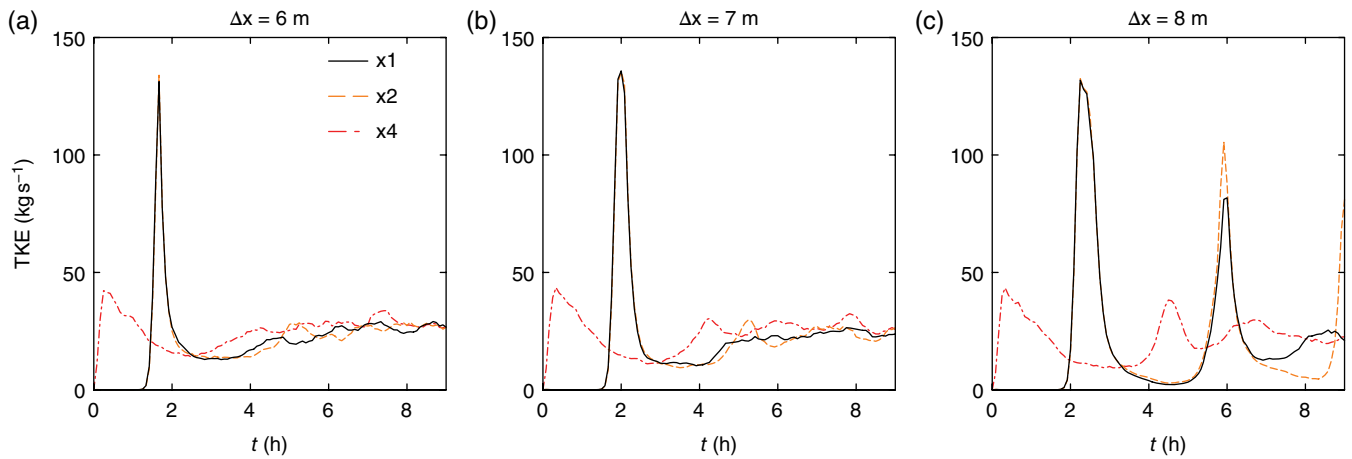
Figure 12. Time traces of vertically integrated turbulent kinetic energy for runs with three different initial perturbation amplitudes and for $\Delta x =$ (a) 6 m, (b) 7 m, and (c) 8 m.
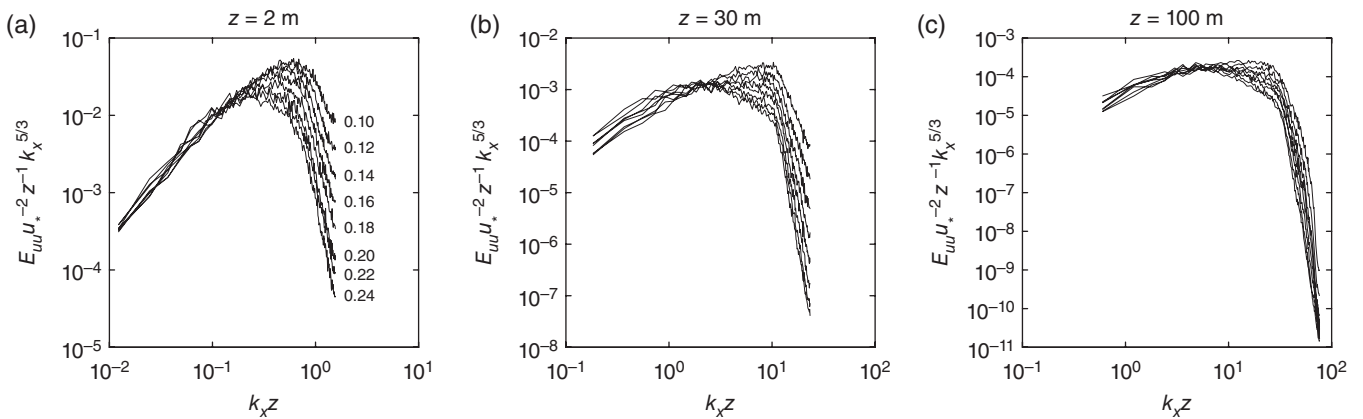
Figure 13. One-dimensional spectra of zonal wind along the zonal, x, direction at heights (a) 2 m, (b) 30 m, and (c) 100 m for different values of the Smagorinsky constant, C_s (shown next to the curves in (a)). The spectra decrease faster at high wavenumbers as C_s increases. The spectra are for runs with $\Delta x = 4$ m and sixth-order advection at the end of the run, $t = 9$ h (no time averaging).
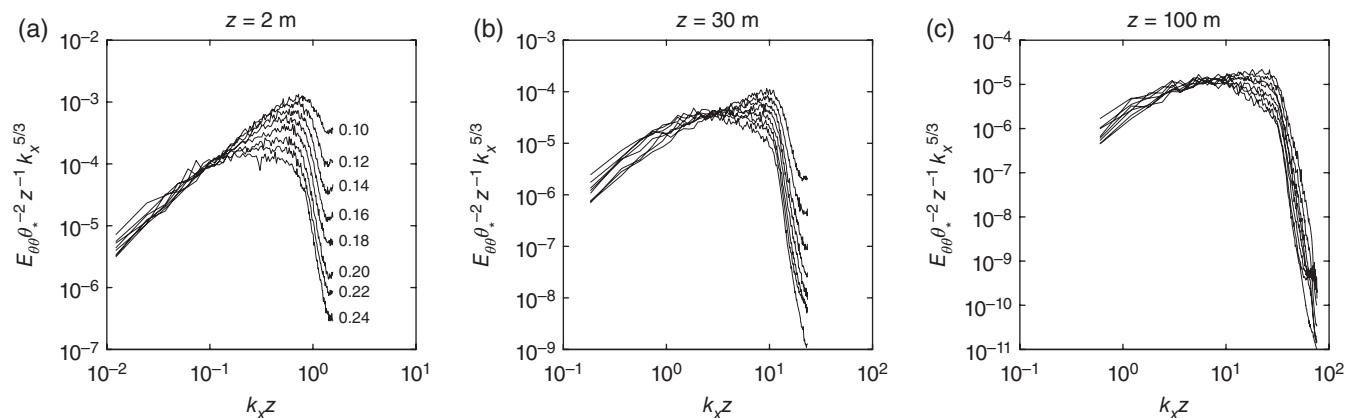
Figure 14. As Figure 13, but for potential temperature.
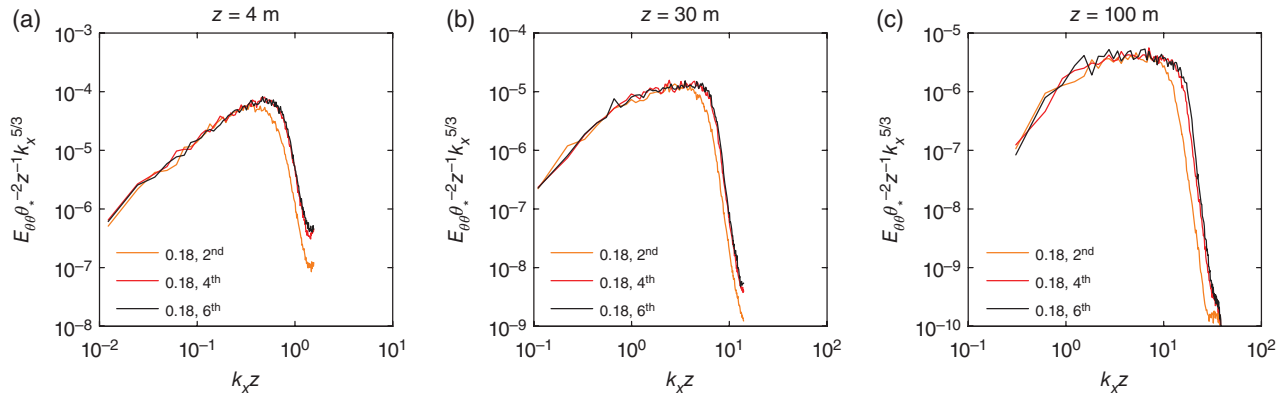
Figure 15. One-dimensional spectra of potential temperature along the zonal, x, direction at three heights (a) 4 m, (b) 30 m, and (c) 100 m for the three advection schemes. The spectra are for runs with $\Delta x = 8$ m and $C_s = 0.18$ at the end of the run, $t = 9$ h (no time averaging).
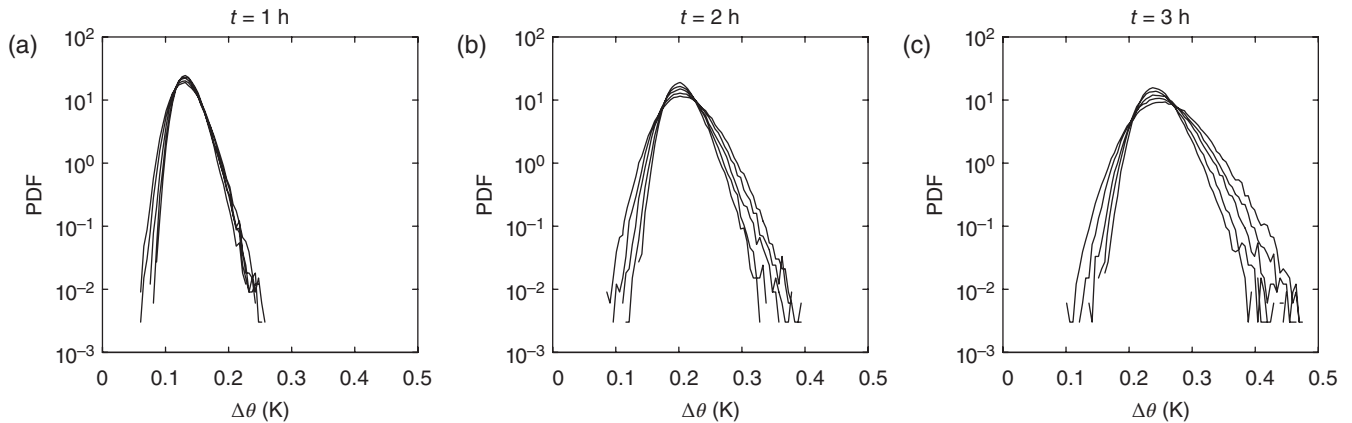
Figure 16. Probability density functions (pdfs) of the potential temperature difference between the first model half-level, $z = \Delta z/2$, and the surface at three times (a) $t = 1$ h, (b) 2 h, and (c) 3 h for five different values of the Smagorinsky constant. The pdfs are for runs with $\Delta x = 8$ m, sixth-order advection and C_s values 0.1, 0.12, 0.14, 0.16, and 0.18. Broader pdfs result from lower values of C_s.

especially in the surface fluxes. The two fine-scale simulations corroborate the main conclusion of the parametric study that the Smagorinsky–Lilly closure exhibits sensitivity to the grid spacing and C_s with some combinations of these parameters yielding accurate results. The optimal model parameter values are likely flow-dependent, e.g. vary with the strength of the stratification, thus a search for the optimal values is not pursued.

5. Conclusions

The present study examines some aspects of the performance of a large-eddy simulation model with the Smagorinsky–Lilly subgrid-scale closure in simulations of a moderately stable boundary layer (Beare *et al.*, 2006). Three model parameters are considered: the grid spacing, the value of the SGS model constant and the order of accuracy (resolving power) of the advection discretization. A reference run with the stretched-vortex SGS model (Chung and Matheou, 2014; Matheou and Chung, 2014) is used to form quantitative metrics for comparison.

The current investigation extends previous studies of LES model performance of 'dry' (without water condensate) boundary layers. A significant characteristic of the present simulations is that all advection schemes are fully conservative and non-dissipative. The second-, fourth- and sixth-order schemes from the family of centred staggered schemes of Morinishi *et al.* (1998) are used.

All three model parameters examined significantly affect the LES results. Depending on the value of the model constant, two main error-producing mechanisms are identified:
(i) For high values of the model constant, $C_s > 0.18$, spurious turbulence collapse, either during the short period of model spin-up, or for the entire simulation, is observed. Global turbulence collapse is interjected by bursts of increased activity. Even though this spurious model characteristic was previously observed

(Jiménez and Cuxart, 2005; Zhou and Chow, 2011; Van de Wiel *et al.*, 2012b), and perhaps expected for low-resolution simulations (Mason and Callen, 1986), it is found to depend on the resolving power of the advection discretization as well. This implies significant discretization and SGS closure interaction.
(ii) For low values of the model constant, numerical discretization errors dominate, leading to accumulation of energy at the small scales and over-prediction of the magnitude of the surface heat flux.

Overall, the fourth- and sixth-order schemes perform better than the second-order scheme. The performance of the second-order scheme is poor and fine grid resolutions and lower values of the model constant are required to maintain turbulence and acceptable differences with respect to the reference run. The differences between the fourth- and sixth-order schemes are small and the increased computational expense of the sixth-order scheme may not be effective in most applications, at least for the low-order statistics considered in this study.

Even though theoretical considerations suggest that C_s should be significantly adjusted based on the resolving power of the advection scheme (e.g. increase by factors of two or more for low-order schemes), the practical range of C_s in the current simulations is limited to a narrow range somewhat higher than the theoretical value, $C_s \approx 0.18$–0.23.

For the current simulations, surface fluxes vary for different model constants, even for finely resolved runs with high-order advection discretizations. Although the impact of the surface fluxes on the boundary-layer dynamics is expected (e.g. Zilitinkevich and Mironov, 1996), the observed differences are relatively large given that the flow configuration is identical. The present runs show the importance of the feedback between boundary-layer turbulence and surface flux.
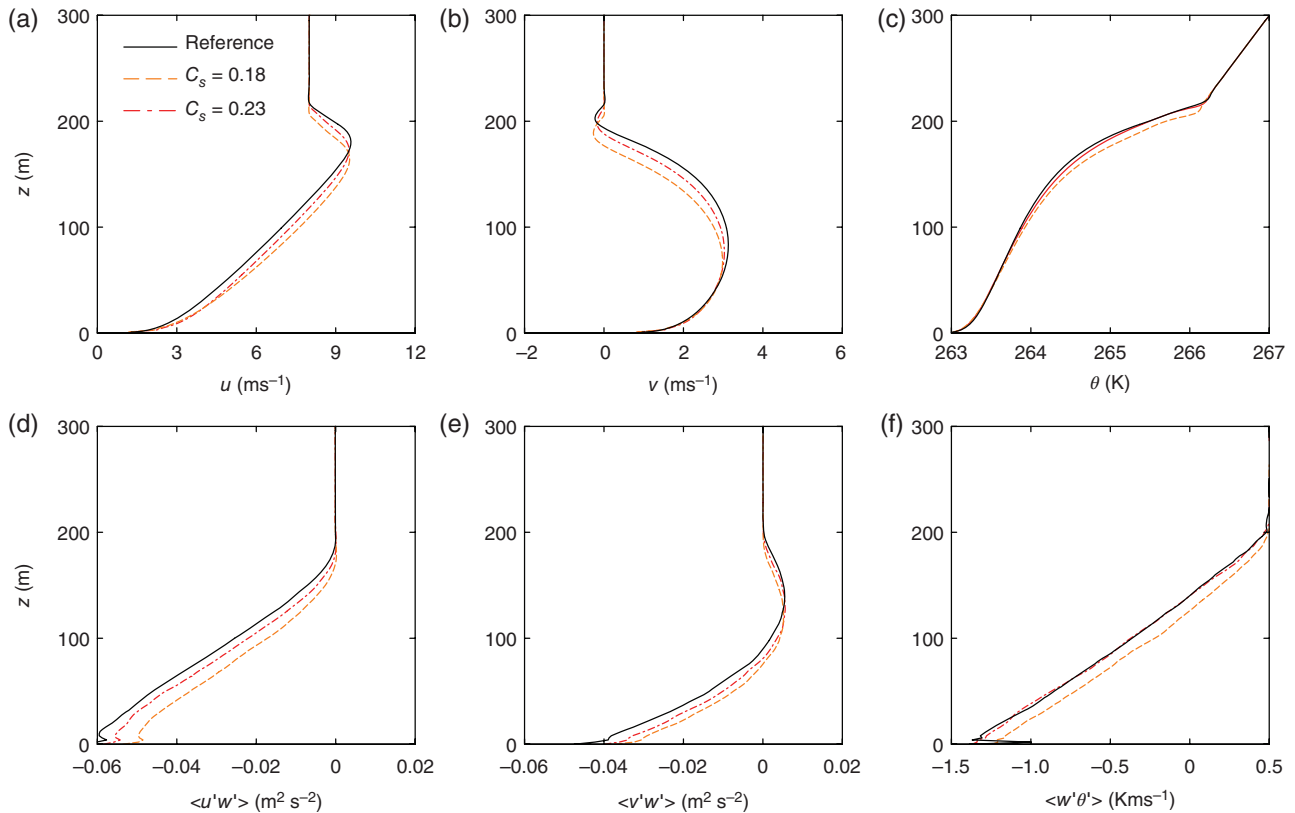
Figure 17. Profiles of (a) zonal wind, (b) meridional wind, (c) potential temperature, (d) u-momentum flux, (e) v-momentum flux and (f) heat flux for the high-resolution runs, $\Delta x = 2$ m. Two Smagorinsky runs with $C_s = 0.18$ and 0.23 and the reference run with the stretched-vortex model are shown. Advection is sixth-order for all runs.
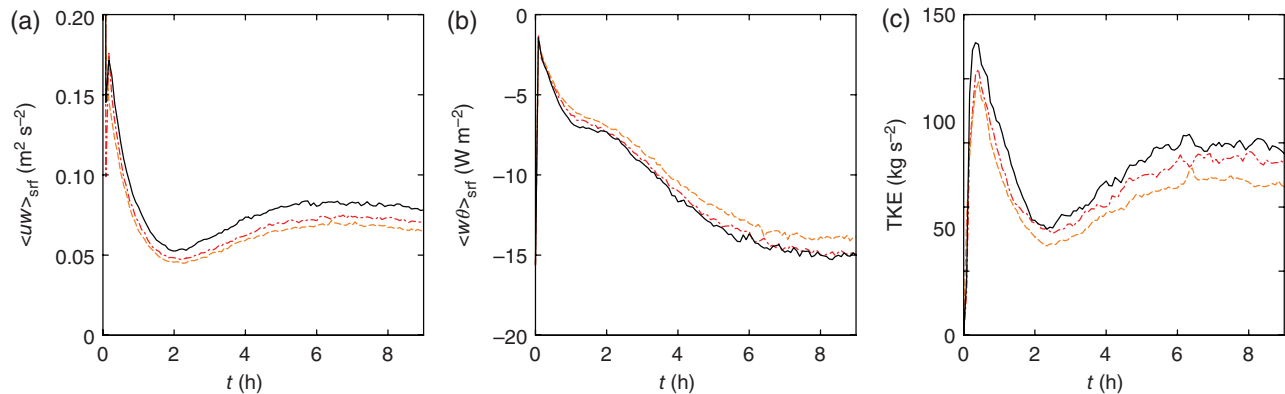
Figure 18. Time traces of (a) surface momentum flux, (b) surface heat flux and (c) vertically integrated TKE for the high-resolution runs, $\Delta x = 2$ m. Line styles are as in Figure 17.

To eliminate the feedback between turbulent flow and surface heat flux, a series of runs with prescribed surface heat flux was carried out. The heat flux from the reference run was used to better facilitate the comparison with the rest of the results. The simulations with prescribed heat fluxes do not show improvement with respect to the reference model. In fact, simulations exhibit turbulence collapse for a broader range of the model constant when the surface heat flux is prescribed compared to runs with dynamically computed fluxes.

Even though the results of the Smagorinsky–Lilly closure show persistent dependence on all model parameters examined, for several of the parameter combinations the differences with respect to the reference model are small. The closure can accurately capture moderately stable flows, in contrast to the conclusions of previous studies. However, the *a priori* choice of the optimal model constant value and grid spacing remains challenging and it is likely flow-dependent. The present closure is purely dissipative (always forward scatter of kinetic energy and potential temperature variance). Therefore, the inclusion of backscatter effects does not appear to be essential in modelling of moderately stable boundary layers.

Acknowledgements

References

Ansorge C, Mellado JP. 2014. Global intermittency and collapsing turbulence in the stratified planetary boundary layer. *Boundary-Layer Meteorol.* **153**: 89–116.

Arakawa A, Lamb VR. 1977. Computational design of the basic dynamical processes of the UCLA general circulation model. In *Methods of Computational Physics*, Chung J. (ed), Vol. 17: 173–265. Academic Press: Singapore.

Basu S, Porté-Agel F. 2006. Large-eddy simulation of stably stratified atmospheric boundary layer turbulence: A scale-dependent dynamic modeling approach. *J. Atmos. Sci.* **63**: 2074−2091.

Basu S, Holtslag AA, Van De Wiel BJ, Moene AF, Steeneveld GJ. 2008. An inconvenient 'truth' about using sensible heat flux as a surface boundary condition in models under stably stratified regimes. *Acta Geophys.* **56**: 88−99.

Batchelor GK. 1953. The condition for dynamical similarity of motions of a frictionless perfect-gas atmosphere. *Q. J. R. Meteorol. Soc.* **79**: 224−235.

Beare RJ, MacVean MK. 2004. Resolution sensitivity and scaling of large-eddy simulations of the stable boundary layer. *Boundary-Layer Meteorol.* **112**: 257−281.

Beare RJ, MacVean MK, Holtslag AAM, Cuxart J, Esau I, Golaz JC, Jimenez MA, Khairoutdinov M, Kosovic B, Lewellen D, Lund TS, Lundquist JK, McCabe A, Moene AF, Noh Y, Raasch S, Sullivan P. 2006. An intercomparison of large-eddy simulations of the stable boundary layer. *Boundary-Layer Meteorol.* **118**: 247−272.

Brown AR, Derbyshire SH, Mason PJ. 1994. Large-eddy simulation of stable atmospheric boundary layers with a revised stochastic subgrid model. *Q. J. R. Meteorol. Soc.* **120**: 1485−1512.

Brown AR, MacVean MK, Mason PJ. 2000. The effects of numerical dissipation in large-eddy simulations. *J. Atmos. Sci.* **57**: 3337−3348.

Bryan GH, Wyngaard JC, Fritsch JM. 2003. Resolution requirements for the simulation of deep moist convection. *Mon. Weather Rev.* **131**: 2394−2416.

Chow FK, Moin P. 2003. A further study of numerical errors in large-eddy simulations. *J. Comput. Phys.* **184**: 366−380.

Chung D, Matheou G. 2012. Direct numerical simulation of stationary homogeneous stratified sheared turbulence. *J. Fluid Mech.* **696**: 434−467.

Chung D, Matheou G. 2014. Large-eddy simulation of stratified turbulence. Part I: A vortex-based subgrid-scale model. *J. Atmos. Sci.* **71**: 1863−1879.

Clark TL. 1979. Numerical simulations with a three-dimensional cloud model: Lateral boundary-condition experiments and multicellular severe storm simulations. *J. Atmos. Sci.* **36**: 2191−2215.

Cuijpers JWM, Duynkerke PG. 1993. Large-eddy simulation of trade-wind cumulus clouds. *J. Atmos. Sci.* **50**: 3894−3908.

Deardorff JW. 1970. A numerical study of three-dimensional turbulent channel flow at large Reynolds numbers. *J. Fluid Mech.* **41**: 453−480.

Deardorff J. 1971. On the magnitude of the subgrid-scale eddy coefficient. *J. Comput. Phys.* **7**: 120−133.

Derbyshire SH. 1990. Nieuwstadt's stable boundary layer revisited. *Q. J. R. Meteorol. Soc.* **116**: 127−158.

Donzis DA, Sreenivasan K, Yeung P. 2010. The Batchelor spectrum for mixing of passive scalars in isotropic turbulence. *Flow Turbul. Combust.* **85**: 549−566.

Esau I. 2004. Simulation of Ekman boundary layers by large-eddy model with dynamic mixed subfilter closure. *Environ. Fluid Mech.* **4**: 273−303.

Fernando HJS. 1991. Turbulent mixing in stratified fluids. *Annu. Rev. Fluid Mech.* **23**: 455−493.

Ghosal S. 1996. An analysis of numerical errors in large-eddy simulations of turbulence. *J. Comput. Phys.* **125**: 187−206.

Harlow FH, Welch JE. 1965. Numerical calculation of time-dependent viscous incompressible flow of fluid with free surface. *Phys. Fluids* **8**: 2182−2189.

Huang J, Bou-Zeid E. 2013. Turbulence and vertical fluxes in the stable atmospheric boundary layer. Part I: A large-eddy simulation study. *J. Atmos. Sci.* **70**: 1513−1527.

Inoue M, Matheou G, Teixeira J. 2014. LES of a spatially developing atmospheric boundary layer: Application of a fringe method for the stratocumulus to shallow cumulus cloud transition. *Mon. Weather Rev.* **142**: 3418−3424.

Ivey GN, Winters KB, Koseff JR. 2008. Density stratification, turbulence, but how much mixing? *Annu. Rev. Fluid Mech.* **40**: 169−184.

Jiménez M, Cuxart J. 2005. Large-eddy simulations of the stable boundary layer using the standard Kolmogorov theory: Range of applicability. *Boundary-Layer Meteorol.* **115**: 241−261.

Kolmogorov AN. 1941. Local structure of turbulence in an incompressible viscous fluid at very high Reynolds numbers. *Dokl. Akad. Nauk SSSR* **30**: 301−305.

Kosovic B, Curry J. 2000. Large-eddy simulation of a quasi-steady, stably stratified atmospheric boundary layer. *J. Atmos. Sci.* **57**: 1052−1068.

Lele SK. 1992. Compact finite difference schemes with spectral-like resolution. *J. Comput. Phys.* **103**: 16−42.

Lilly DK. 1962. On the numerical simulation of buoyant convection. *Tellus* **14**: 148−172.

Lilly DK. 1966. *On the Application of the Eddy Viscosity Concept in the Inertial Sub-Range of Turbulence*, NCAR manuscript 123. National Center for Atmospheric Research: Boulder, CO.

Lilly DK. 1967. 'The representation of small-scale turbulence in numerical simulation experiments'. In *Proceedings of the IBM Scientific Computing Symposium on Environmental Science. Yorktown Heights, NY*, pp. 195−210.

Liu Z, Thorpe S, Smyth W. 2012. Instability and hydraulics of turbulent stratified shear flows. *J. Fluid Mech.* **695**: 235−256.

Lomax H, Pulliam TH, Zingg DW. 2003. *Fundamentals of Computational Fluid Dynamics*. Springer: Berlin.

Mahrt L. 2011. The near-calm stable boundary layer. *Boundary-Layer Meteorol.* **140**: 343−360.

Mason PJ, Brown AR. 1999. On subgrid models and filter operations in large-eddy simulations. *J. Atmos. Sci.* **56**: 2101−2114.

Mason PJ, Callen NS. 1986. On the magnitude of the subgrid-scale eddy coefficient in large-eddy simulations of turbulent channel flow. *J. Fluid Mech.* **162**: 439−462.

Mason PJ, Thomson DJ. 1992. Stochastic backscatter in large-eddy simulations of boundary layers. *J. Fluid Mech.* **242**: 51−78.

Matheou G, Bowman KW. 2016. A recycling method for the large-eddy simulation of plumes in the atmospheric boundary layer. *Environ. Fluid Mech.* **16**: 69−85.

Matheou G, Chung D. 2014. Large-eddy simulation of stratified turbulence. Part II: Application of the stretched-vortex model to the atmospheric boundary layer. *J. Atmos. Sci.* **71**: 4439−4460.

Matheou G, Chung D, Nuijens L, Stevens B, Teixeira J. 2011. On the fidelity of large-eddy simulation of shallow precipitating cumulus convection. *Mon. Weather Rev.* **139**: 2918−2939.

Morinishi Y, Lund TS, Vasilyev OV, Moin P. 1998. Fully conservative higher-order finite-difference schemes for incompressible flow. *J. Comput. Phys.* **143**: 90−124.

Nieuwstadt FT. 1984. The turbulent structure of the stable, nocturnal boundary layer. *J. Atmos. Sci.* **41**: 2202−2216.

Ogura Y, Phillips NA. 1962. Scale analysis of deep and shallow convection in the atmosphere. *J. Atmos. Sci.* **19**: 173−179.

Ohya Y, Nakamura R, Uchida T. 2008. Intermittent bursting of turbulence in a stable boundary layer with low-level jet. *Boundary-Layer Meteorol.* **126**: 349−363.

Orszag SA. 1971. On the elimination of aliasing in finite-difference schemes by filtering high-wavenumber components. *J. Atmos. Sci.* **28**: 1074.

Piacsek SA, Williams GP. 1970. Conservation properties of convection difference schemes. *J. Comput. Phys.* **6**: 392−405.

Poulos GS, Burns SP. 2003. An evaluation of bulk *Ri*-based surface layer flux formulas for stable and very stable conditions with intermittent turbulence. *J. Atmos. Sci.* **60**: 2523−2537.

Pullin DI. 2000. A vortex-based model for the subgrid flux of a passive scalar. *Phys. Fluids* **12**: 2311−2316.

Riley JJ, Lelong MP. 2000. Fluid motions in the presence of strong stable stratification. *Annu. Rev. Fluid Mech.* **32**: 613−657.

Saddoughi SG, Veeravalli SV. 1994. Local isotropy in turbulent boundary layers at high Reynolds number. *J. Fluid Mech.* **268**: 333−372.

Schmidt H, Schumann U. 1989. Coherent structure of the convective boundary layer derived from large-eddy simulations. *J. Fluid Mech.* **200**: 511−562.

Schubert J. 1977. Acoustic detection of momentum transfer during the abrupt transition from a laminar to a turbulent atmospheric boundary layer. *J. Appl. Meteorol.* **16**: 1292−1297.

Schumann U. 1985. Algorithms for direct numerical simulation of shear-periodic turbulence. In *Lecture Notes in Physics*, Soubbaramayer, Boujot JP. (eds.), Vol. 218: 492−496. Springer: Berlin.

Smagorinsky J. 1963. General circulation experiments with the primitive equations. I. The basic experiment. *Mon. Weather Rev.* **91**: 99−164.

Smagorinsky J. 1993. Some historical remarks on the use of nonlinear viscosities. In *Large-Eddy Simulation of Complex Engineering and Geophysical Flows*, Galperin B, Orszag SA. (eds.): 3−36. Cambridge University Press: New York, NY.

Sommeria G. 1976. Three-dimensional simulation of turbulent processes in an undisturbed trade wind boundary layer. *J. Atmos. Sci.* **33**: 216−241.

Sommeria G, Deardorff JW. 1977. Subgrid-scale condensation in models of non-precipitating clouds. *J. Atmos. Sci.* **34**: 344−355.

Spalart PR, Moser RD, Rogers MM. 1991. Spectral methods for the Navier−Stokes equations with one infinite and two periodic directions. *J. Comput. Phys.* **96**: 297−324.

Stoll R, Porté-Agel F. 2008. Large-eddy simulation of the stable atmospheric boundary layer using dynamic models with different averaging schemes. *Boundary-Layer Meteorol.* **126**: 1−26.

Sullivan PG, Patton EG. 2011. The effect of mesh resolution on convective boundary layer statistics and structures generated by large-eddy simulation. *J. Atmos. Sci.* **68**: 2395−2415.

Van de Wiel B, Moene A, Jonker H. 2012a. The cessation of continuous turbulence as precursor of the very stable nocturnal boundary layer. *J. Atmos. Sci.* **69**: 3097−3115.

Van de Wiel B, Moene A, Jonker H, Baas P, Basu S, Donda J, Sun J, Holtslag A. 2012b. The minimum wind speed for sustainable turbulence in the nocturnal boundary layer. *J. Atmos. Sci.* **69**: 3116−3127.

Voelkl T, Pullin DI, Chan DC. 2000. A physical-space version of the stretched-vortex subgrid-stress model for large-eddy simulation. *Phys. Fluids* **12**: 1810−1825.

Zhou B, Chow FK. 2011. Large-eddy simulation of the stable boundary layer with explicit filtering and reconstruction turbulence modeling. *J. Atmos. Sci.* **68**: 2142−2155.

Zilitinkevich S, Mironov DV. 1996. A multi-limit formulation for the equilibrium depth of a stably stratified boundary layer. *Boundary-Layer Meteorol.* **81**: 325−351.

Zilitinkevich S, Elperin T, Kleeorin N, Rogachevskii I, Esau I, Mauritsen T, Miles M. 2008. Turbulence energetics in stably stratified geophysical flows: Strong and weak mixing regimes. *Q. J. R. Meteorol. Soc.* **134**: 793−799.